

Ocean Current Estimated From X-Band Radar Sea Surface Images

Rune Gangeskar

Abstract—Sea surface currents can be derived from X-band radar sea surface images. The basic theory is previously known. However, in practice, the current estimates may be deteriorated by several sources of error. Trials with real radar data previously indicated that some further research was required to obtain reasonable current estimates. A current measurement algorithm has been derived, which compensates for some of the errors. In addition, a novel current measurement algorithm has been derived, using a slightly different approach to the problem, which makes it possible to avoid several of the sources of errors. Signal analysis is used in combination with knowledge about the properties of the three-dimensional image spectrum. The algorithms are tested on real radar data and compared to simultaneous microwave dual-frequency measurements and wind measurements. In addition, the estimated currents are evaluated by comparing to values obtained from the tidal model. Finally, the sea surface current vector field is estimated, with a resolution of 256 m, to provide more detailed information about the current within the radar image, which constitutes an area of many square kilometers.

Index Terms—Current, discrete Fourier transforms, dispersion relationship, error analysis, image processing, radar, sea surface, signal processing.

I. INTRODUCTION

SEA SURFACE currents can be derived from X-band radar sea surface images. Three-dimensional (3-D) wavenumber/frequency spectra are obtained by performing 3-D fast Fourier transforms (FFTs) on the images [1]. When no current is present, the power for a given frequency value should be located on a circle in the wavenumber space, determined by the dispersion relationship [2]. The dispersion relationship for gravity waves is given approximately as

$$\omega_0^2 \approx g|\vec{k}| \tanh(|\vec{k}|d) \quad (1)$$

where ω_0 is the wave frequency, \vec{k} is the wavenumber vector, d is the water depth, and g is the gravitational acceleration. If there is a surface current \vec{U} relative to the radar, a Doppler frequency shift is introduced in the wave frequency

$$\omega = \omega_0 + \vec{k} \cdot \vec{U}. \quad (2)$$

The Doppler shift causes the energy in the 3-D spectra to be located on ellipses, rather than circles. By estimating the shapes of the ellipses, an estimate of the current vector \vec{U} can be calculated.

Several sources of error, such as limited spectral resolution, nonuniform distribution of spectrum energy, geometrical factors, and noise, contribute to deteriorate the current estimate. Many of these errors would theoretically be zero if the spectral resolution was infinite. However, in practice, this is never the case because it would require infinite extent in both the temporal and spatial dimensions. Up to now, trials with real radar data have indicated that some further research is required to obtain reasonable current estimates [3].

A novel current measurement algorithm has been derived, referred to as Algorithm A, which compensates for the main sources of errors. The algorithm is tested on real radar data [4]. The X-band radar current estimates is shown to comply reasonably well with simultaneous MIROS Doppler wave radar measurements and wind measurements. The MIROS Doppler wave radar ([5] and [6]) uses the dual-frequency method for current measurements. Harmonic analysis is performed on the estimated currents to verify the accuracy of the measured tidal movement.

A novel and somewhat different method to estimate the current from the X-band radar images is discussed as well and is referred to as Algorithm B. The power frequency spectrum for every single wavenumber can be estimated using *a priori* information about the integrated wavenumber spectrum shape and resolution. Then, by adding various Doppler shifts and convolving with the temporal spectral response function, it is possible to perform a least squares fit to find the underlying current in the measured 3-D wavenumber/frequency spectrum.

The advantage of Algorithm B is that several of the sources of error previously considered are avoided, especially the undesirable influence from the wave spectrum shape and the FFT spectral response function. Algorithm B also provides a basis for creating more robust and reliable routines for noise removal.

Until now, one average current vector estimate has been derived from the sea surface area covered by the radar images. However, it is possible to evaluate current vectors in various locations in the radar images, thereby obtaining a current vector field with information about the current pattern inside the area covered by the radar images. This is considered at the end of this paper.

II. CURRENT ESTIMATION WITH IMPROVED TRADITIONAL ALGORITHM

This section considers an improved algorithm, referred to as Algorithm A, which is directly based on the traditional method described by [2] and [3].

Manuscript received June 22, 2001; revised December 10, 2001. This work was supported by MIROS A/S and the Norwegian Research Council.

R. Gangeskar is with MIROS A/S, N-1372 Asker, Norway (e-mail: rg@miros.no).

Publisher Item Identifier S 0196-2892(02)04606-5.

A. Basic Principles

The current \vec{U} may be estimated, using a weighted least squares method [3], by minimizing the function

$$J = \sum_{\omega=0}^{\omega_M} \sum_{k_x=-k_{xN}}^{k_{xN}} \sum_{k_y=-k_{yN}}^{k_{yN}} (\Delta\omega)^2 E(k_x, k_y, \omega) \quad (3)$$

where

$$\Delta\omega = \omega - \sqrt{g|\vec{k}|} - k_x U_x - k_y U_y \quad (4)$$

assuming deep water compared to the wave length, that is

$$|\vec{k}|d \gg 1 \quad (5)$$

in (1). $E(k_x, k_y, \omega)$ is the 3-D wavenumber/frequency spectrum, and U_x and U_y are the x and y components of \vec{U} . The solution of (3) with respect to U_x and U_y is

$$\begin{bmatrix} U_x \\ U_y \end{bmatrix} = \begin{bmatrix} \sum E k_x^2 & \sum E k_x k_y \\ \sum E k_x k_y & \sum E k_y^2 \end{bmatrix}^{-1} \cdot \begin{bmatrix} \sum E(\omega - \sqrt{g|\vec{k}|}) k_x \\ \sum E(\omega - \sqrt{g|\vec{k}|}) k_y \end{bmatrix}. \quad (6)$$

B. Sources of Error

Various sources of error will be discussed in Sections II-B1–II-B5.

1) *Resolution*: The limited spectral resolution in the 3-D wavenumber/frequency space may be improved by interpolation in the frequency dimension [3]. A more precise frequency value may be estimated by

$$\hat{f} = f_1 \pm \Delta f \frac{\sqrt{\frac{a_2}{a_1}}}{1 + \sqrt{\frac{a_1}{a_2}}} \quad (7)$$

where f_1 is the frequency associated with the power peak with amplitude a_1 , f_2 is the greatest neighbor with amplitude a_2 , and Δf is the frequency resolution. The \pm sign depends on whether the greatest neighbor is located above or below the peak frequency respectively. Equation (7) is obtained simply by using the fact that a single line in the spectrum gives response in two neighboring frequencies, due to the FFT giving the response of a $\sin x/x$ filter with 3 dB overlap. The assumption of a single line is not necessarily valid, as the succeeding discussion indicates. Equation (7) also takes into account the result of the FFT has to be squared to obtain the power spectrum.

2) *Wave Spectrum Shape and FFT Filter Response*: The sea surface wave power is sorted with respect to wavenumber by the 2-D spatial FFT. The power frequency spectrum of a wavenumber bin is determined by the wave power distribution (i.e., the wavenumber spectrum shape), the FFT spectral response function, the wavenumber resolution, and in addition the Doppler frequency shift due to surface currents. Thus, the estimated frequency \hat{f} in (7) will be undesirably affected by other factors than the Doppler shift. Both the frequency and wavenumber resolution determine the effect of these influences.

When the frequency resolution Δf is sufficiently good, no frequency interpolation is needed. The above mentioned effects are in this situation negligible.

When the frequency resolution requires interpolation, the wavenumber resolution, Δk , determines the effects of the above mentioned unwanted influences on the estimated frequency. The different cases may be roughly summed up as follows.

- With a very good wavenumber resolution, $\Delta k_f \ll \Delta f$, the power frequency spectrum for one single wavenumber becomes very narrow banded, according to the dispersion relationship in (1). Δk_f is the wavenumber resolution calculated in temporal frequency using the dispersion relationship. The interpolation defined by (7) will for this case be a good estimate of the real frequency, without being significantly influenced either by the wave spectrum shape, nor the FFT filter response.
- With a very poor wavenumber resolution, $\Delta k_f \gg \Delta f$, the power frequency spectrum for one single wavenumber will have a shape which is highly influenced by the wave spectrum shape, together with the shape of the FFT spectral response function. Hence, the amplitudes a_1 and a_2 in (7) will be affected by the Doppler shift due to surface currents, the wave spectrum shape, and the FFT spectral response. Anyway, the poor wavenumber resolution itself will be the strongest cause of the uncertainties in the current estimates for this case, due to the lack of information about which wavenumber belongs to the estimated frequency \hat{f} .
- With a wavenumber resolution of the same order of magnitude as the frequency resolution, the power frequency spectrum for one single wavenumber will also have a shape which is highly influenced by the wave spectrum shape, and the shape of the FFT spectral response function. In this case, the wavenumber resolution is not the only factor reducing the accuracy. Taking the knowledge about the integrated wavenumber spectrum shape and the FFT spectral response function into account, it should be possible to perform some kind of weighting of the 3-D wavenumber/frequency spectrum to remove some of the undesirable influence on a_1 and a_2 in (7). However, this will be a rather complex calculation and is not to be considered further in this paper.

3) *Geometry*: The wave spectrum power is located around an elliptic shell in the 3-D wavenumber/frequency space. The spectrum power is somewhat scattered, due to the limited spectral resolution. The spectrum points are defined on a Cartesian grid. Thus, geometrical factors together with the spectrum power location constitute an estimation error when fitting an elliptic shell to the spectrum points.

4) *Nonlinearity in the Fitting*: For a given current, the power contribution to the square deviation in (3) depends on the wavenumber. Power associated with high wavenumbers contributes more to the square deviation than power associated with low wavenumbers does. This may be avoided by modifying the error function in (3) as

$$J = \sum_{\omega=0}^{\omega_M} \sum_{k_x=-k_{xN}}^{k_{xN}} \sum_{k_y=-k_{yN}}^{k_{yN}} (\Delta\omega_M)^2 E(k_x, k_y, \omega) \quad (8)$$

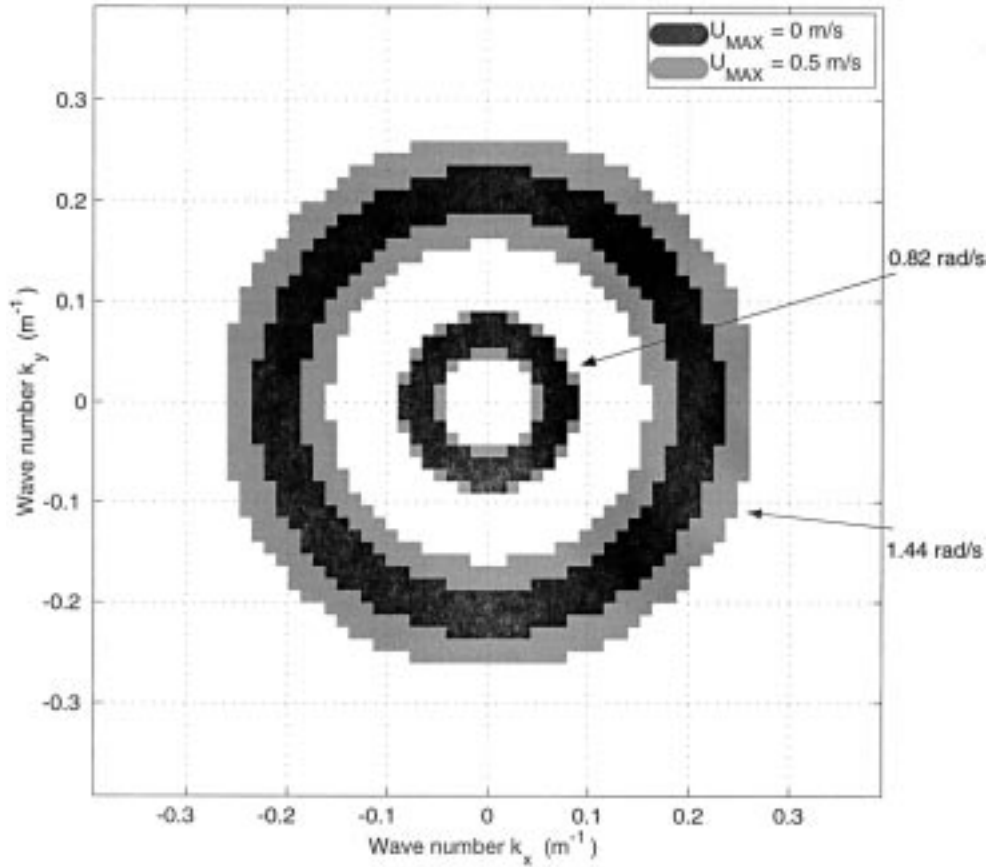


Fig. 1. Dispersion filter for two wavenumber planes corresponding to the frequencies of 0.82 rad/s (inner circle) and 1.44 rad/s (outer circle), with $\Delta k = 0.012 \text{ m}^{-1}$ and $\Delta\omega = 0.10 \text{ rad/s}$. Two different values of U_{\max} are shown in the figure: 0 m/s and 0.5 m/s.

where

$$\Delta\omega_M = \frac{\omega - \sqrt{g|\vec{k}|} - k_x U_x - k_y U_y}{|\vec{k}|}. \quad (9)$$

Tests performed on real data, however, indicate that the current estimates are not improved by using the modified error function in (8) and (9). Doppler shift at low wavenumbers has a higher relative uncertainty. Thus, the gain of using the modified error function is compensated by putting higher weights on the low wavenumbers.

5) *Noise*: Typical North Sea surface currents are in the order of magnitude of 10 cm/s, which is typically only a few percent of the wave speed, and small compared to the inaccuracy of the image position due to the radar mechanical position tolerance. The uncertainty in the image location for every single radar scan may typically be a few meters. Several sources of noise will contribute strongly to the spectrum power, which make it important to be able to remove noise. Dispersion filtering is suitable, because the 3-D spectrum is available.

a) *Dispersion filtering*: When creating the dispersion filter, it has to be taken into account that the energy will be located on ellipses, rather than circles, when there is a current present. This will require a more wide banded filter depending on the maximum expected current speed, as long as the current speed and direction are unknown. Assuming a maximum cur-

rent speed U_{\max} , and the deep water condition, one realization of the dispersion filtering process may be defined as

$$E_D(k_x, k_y, \omega) = \begin{cases} E, & |\vec{k}| \in [B_n, B_p] \\ 0, & \text{otherwise} \end{cases} \quad (10)$$

where

$$B_n = \frac{\left(\omega - \frac{\Delta\omega}{2} - U_{\max} \frac{\omega^2}{g}\right)^2}{g} - \sqrt{2} \frac{\Delta k}{2} \quad (11)$$

and

$$B_p = \frac{\left(\omega + \frac{\Delta\omega}{2} + U_{\max} \frac{\omega^2}{g}\right)^2}{g} + \sqrt{2} \frac{\Delta k}{2}. \quad (12)$$

Δk is the wavenumber resolution, $\Delta\omega$ is the frequency resolution, and it is assumed that the expression in brackets in (11) is not negative. For negative values in the brackets, $B_n = 0 \text{ m}^{-1}$. Because one half of the resolution is considered in every dimension in both the negative and positive directions, no signal peaks in the power spectrum are removed by the filter.

Fig. 1 illustrates a realization of the dispersion filter for two wavenumber planes corresponding to the frequencies of 0.82 and 1.44 rad/s, with $\Delta k = 0.012 \text{ m}^{-1}$ and $\Delta\omega = 0.10 \text{ rad/s}$. These resolutions are used throughout this paper. The dispersion filter does only contain values of 1 or 0, depending on whether the signal is passed through or not. Areas containing 1 are in-

indicated by the gray and black circles. Two different values of U_{\max} are shown in the figure, and as discussed above, the filter corresponding to the highest value of U_{\max} is the widest.

It is obvious that the dispersion filtering will be very inefficient if U_{\max} is large, because the filter must be very wide, allowing all power through. Thus, there may be a need for other methods of noise filtering when estimating currents at locations with high current magnitudes.

b) Requiring an SNR: An additional or alternative method for noise filtering is to require the power frequency spectrum of every single wavenumber to have a minimum signal-to-noise ratio (SNR). If the minimum SNR is not obtained for a wavenumber (k_{x_l}, k_{y_m}) , the corresponding power can be regarded as noise and set equal to 0. This may be done before the interpolation and dispersion filtering, for instance

$$E_{\text{SNR}}(k_{x_l}, k_{y_m}, \omega) = \begin{cases} E, & \max(E(k_{x_l}, k_{y_m}, \omega)) > \eta \\ 0, & \text{otherwise} \end{cases} \quad (13)$$

where the threshold

$$\eta = c \cdot \max(E(k_{x_l}, k_{y_m}, \omega_A)), \quad A \in A_1 \setminus A_2 \quad (14)$$

where \max is the maximum function, c is a factor specifying the SNR, and the sets A_1 and A_2 are defined by

$$\begin{aligned} A_1 &\in \{1, 2, \dots, N\} \\ A_2 &\in \{n-1, n, n+1\} \end{aligned} \quad (15)$$

where n is the frequency index corresponding to maximum power for wavenumber (k_{x_l}, k_{y_m}) . This means that the threshold η for a given wavenumber is determined by the maximum power value outside the peak power area.

III. CURRENT ESTIMATION WITH NOVEL ALGORITHM

This section describes a novel algorithm, referred to as Algorithm B, for current estimation from X-band radar images.

$E(\vec{k}, \omega)$, or $E(k_x, k_y, \omega)$, is a discrete spectrum, due to the nature of the FFT. The integrated wavenumber spectrum $S(\vec{k})$ is obtained by summing $E(\vec{k}, \omega)$ over all positive frequencies, and performing multiplication by 2, due to the symmetry in the spectrum. Only the part of the wavenumber/frequency space corresponding to positive frequencies is considered in the following.

A. Power Frequency Spectrum for a Single Wavenumber Bin

The wavenumber power contents of a wavenumber bin can be estimated using the estimated wavenumber spectrum $S(\vec{k})$ and information about the wavenumber spectrum resolution. The resolution in the x -dimension Δk_x is given by

$$\Delta k_x = \frac{2\pi}{L_x} \quad (16)$$

where L_x is the image extent. By interpolating the spectrum $S(\vec{k})$, a continuous wavenumber spectrum $S^C(\vec{k})$ is obtained. $S^C(\vec{k})$ is our best estimate of the real wavenumber spectrum. The superscript C is used to indicate a continuous function in the rest of this paper.

Performing a 2-D FFT on the Cartesian images is equivalent to applying a filter bank, in which the individual filters have a

certain response function $R_{\vec{k}^0}^C(\vec{k})$, which is approximately given by

$$R_{\vec{k}^0}^C(\vec{k}) = \frac{\sin^2\left(\pi \frac{k_x - k_x^0}{\Delta k_x}\right)}{\left(\pi \frac{k_x - k_x^0}{\Delta k_x}\right)^2} \cdot \frac{\sin^2\left(\pi \frac{k_y - k_y^0}{\Delta k_y}\right)}{\left(\pi \frac{k_y - k_y^0}{\Delta k_y}\right)^2} \quad (17)$$

where \vec{k}^0 is the wavenumber of interest. This response function can be calculated for instance by using the methods described in [7] or [8]. A multiplication in wavenumber domain is equivalent to a convolution in the spatial domain. Thus, the power contents of a wavenumber bin is obtained by multiplying the real wavenumber spectrum by the response function $R_{\vec{k}^0}^C(\vec{k})$ for the current wavenumber bin

$$P_{\vec{k}^0}^C(\vec{k}) = S^C(\vec{k}) R_{\vec{k}^0}^C(\vec{k}). \quad (18)$$

The wavenumber power is transformed to frequency power using the dispersion relationship. Assuming deep water and zero current, it is given by

$$\omega^2 = g|\vec{k}| \quad (19)$$

where ω is the wave frequency and g is the gravitational acceleration. The power frequency spectrum for a single wavenumber bin is given by

$$S_{\vec{k}^0}^C(\omega) = \frac{2\omega^3}{g^2} \int_0^{2\pi} P_{\vec{k}^0}^C\left(\frac{\omega^2}{g}, \theta\right) d\theta \quad (20)$$

quite similar to the methods described in [9]. θ is the bearing of \vec{k} .

To obtain the same frequency resolution for the estimated power $S_{\vec{k}^0}^C(\omega)$ as the power obtained from the FFT, $S_{\vec{k}^0}^C(\omega)$ is multiplied by the FFT response function for every single frequency bin. The frequency resolution $\Delta\omega$ for the FFT is given by

$$\Delta\omega = \frac{2\pi}{T} \quad (21)$$

where T is the duration of the time series. The response function is given by

$$R_{\omega^0}^C(\omega) = \frac{\sin^2\left(\pi \frac{\omega - \omega^0}{\Delta\omega}\right)}{\left(\pi \frac{\omega - \omega^0}{\Delta\omega}\right)^2}, \quad (22)$$

where ω_0 is the frequency of interest. Then, the power in one single frequency bin is given by

$$P_{\vec{k}^0}(\omega_0) = \int_{-\infty}^{\infty} S_{\vec{k}^0}^C(\omega) R_{\omega^0}^C(\omega) d\omega. \quad (23)$$

The complete estimated discrete power frequency spectrum, $S_{\vec{k}^0}(\omega)$, is obtained by evaluating the power for every single frequency bin using (23).

B. Estimating Current

A Doppler frequency shift, ω_D , is subtracted from the estimated power frequency spectrum in (23)

$$P_{\vec{k}^0}(\omega_0, \omega_D) = \int_{-\infty}^{\infty} S_{\vec{k}^0}^C(\omega - \omega_D) R_{\omega^0}^C(\omega) d\omega. \quad (24)$$

A discrete power frequency spectrum $S_{\vec{k}_0}(\omega, \omega_D)$, included Doppler frequency shift, is obtained with the same procedure as previously. Thus, the Doppler shift in the measured 3-D spectrum $E(\vec{k}, \omega)$ can be found by minimizing the rms deviation for each wavenumber, $\Delta_{\text{rms}}(\vec{k})$, with respect to the Doppler shift ω_D

$$\Delta_{\text{rms}}(\vec{k}, \omega_D) = \sqrt{\sum_{n=1}^N (S_{\vec{k}_0}(\omega_n, \omega_D) - E(\vec{k}, \omega_n))^2} \quad (25)$$

where N is the number of positive frequency bins.

The current is estimated using a least squares method, equivalent to the method in (6), by

$$\begin{bmatrix} U_x \\ U_y \end{bmatrix} = \begin{bmatrix} \sum E k_x^2 & \sum E k_x k_y \\ \sum E k_x k_y & \sum E k_y^2 \end{bmatrix}^{-1} \cdot \begin{bmatrix} \sum E \omega_D k_x \\ \sum E \omega_D k_y \end{bmatrix}. \quad (26)$$

C. Noise Removal

Some sort of dispersion filtering can be used for noise removal. This can be realized by rejecting wavenumbers giving a Doppler shift ω_D out of range of the dispersion filter. It should also be possible to create quite sophisticated routines for noise removal based on comparing the shapes of $S_{\vec{k}_0}(\omega, \omega_D)$ and $E(\vec{k}, \omega)$ in (25), for instance.

D. Principal Theoretical Advantages of Novel Algorithm

One of the reasons for creating this novel Algorithm B is the possibility to avoid some of the sources of error connected to Algorithm A. The unwanted influence from the wave spectrum shape and the FFT response function, as discussed for Algorithm A, is avoided by taking the wavenumber spectrum $S^C(\vec{k})$ and the FFT response functions [(17) and (22)] into account when estimating the current. This also makes it possible to avoid the errors of Algorithm A connected to the interpolation. The geometrical factors discussed in connection with Algorithm A should no longer be an actual problem with Algorithm B. As mentioned in Section III-C, an additional advantage of Algorithm B is the possibility to create more sophisticated routines for noise removal.

A disadvantage of Algorithm B is a significantly increased computation time.

IV. ESTIMATING THE SEA SURFACE VECTOR FIELD

Cartesian image sections with dimensions 512×512 m, equally spaced with 256-m separation, are extracted from the polar radar images. For every Cartesian section, the surface current vector is estimated using Algorithm A as described above.

V. RESULTS

A. Collecting and Processing Radar Images

The sea-clutter images used for testing are collected with a standard X-band navigation radar from the Gullfaks C oil production platform in the North Sea [4]. In the same period, current data have been collected with a MIROS Doppler Wave

Radar Mk II ([5] and [6]), and these data are used as reference data. Information about the wind speed and direction 10 m above mean sea level is available from the same site.

B. Evaluation of Time Series

Fig. 2 shows estimated current data for February 1999 (red line) compared to the wave radar reference (blue line) and the measured wind at the site (green line). A 50° hysteresis is added to prevent the direction values from oscillating between 0° and 360° . Algorithm A including interpolation in frequency dimension, dispersion filtering, and the additional noise filtering described above [(13) with $c = 2$] is used to estimate the current. The effect of the interpolation is very small, due to the wavenumber resolution being in the same order of magnitude as the frequency resolution, as mentioned above. 2.5% of the wind magnitude is used in the comparison with the current magnitude. Values between 2% [10] and 3.5% [2] can be reasonable. Forty-five degrees is added to the wind direction to compensate for the deflection due to the Coriolis effect [10], to make the wind direction more comparable to the current directions.

The current direction estimates from the X-band radar images are quite consistent with the reference data. The magnitude estimates are not as good as the direction estimates, but the trends have many similarities with the reference data. In some periods there are larger deviations, for instance the large deviation in current magnitude between 02/04 and 02/06. This may be due to heavy precipitation, disturbing the X-band radar more than the Doppler Wave Radar, because the range of observation is significantly higher (1.5 km) for the X-band radar than for the Doppler radar (300 m). In addition, the electromagnetic wavelength used by the Doppler radar is longer (5 cm) than that used by the X-band radar (3 cm). Another possible reason for the deviation between the two sensors is the fact that they measure at different sea surface wave lengths. This implies that the current estimates from the two radars may be weighted averages of the surface current over two different depths [2].

The current time series estimated with Algorithm B is very similar to the estimates of Fig. 2, despite the fact that the two algorithms differ in several important ways, as discussed previously. Algorithm B also does not use any noise removal routine in addition to the dispersion filtering. Algorithm B used for the current estimation corresponds to the methods described above, including dispersion filtering.

The parameters of the tidal current ellipses for the constituents M2, S2, N2, and K1 are evaluated (Table I). The estimated X-band radar values using Algorithm A and B are compared to the values predicted by the tidal model [11]. The values obtained by the Doppler wave radar are evaluated as well. The amplitudes of the tidal constituents estimated from the X-band radar images are considerably smaller than the amplitudes predicted by the tidal model, and also less than the amplitudes estimated by the wave radar. The angle (θ), however, is quite consistent for the various measurement techniques. Algorithm B seems to be a little more precise than Algorithm A when comparing the ellipses' angles to the predicted ones, but a little more imprecise when comparing the magnitudes. The error in the direction of rotation for S2 estimated with Algorithm A is corrected by Algorithm B.

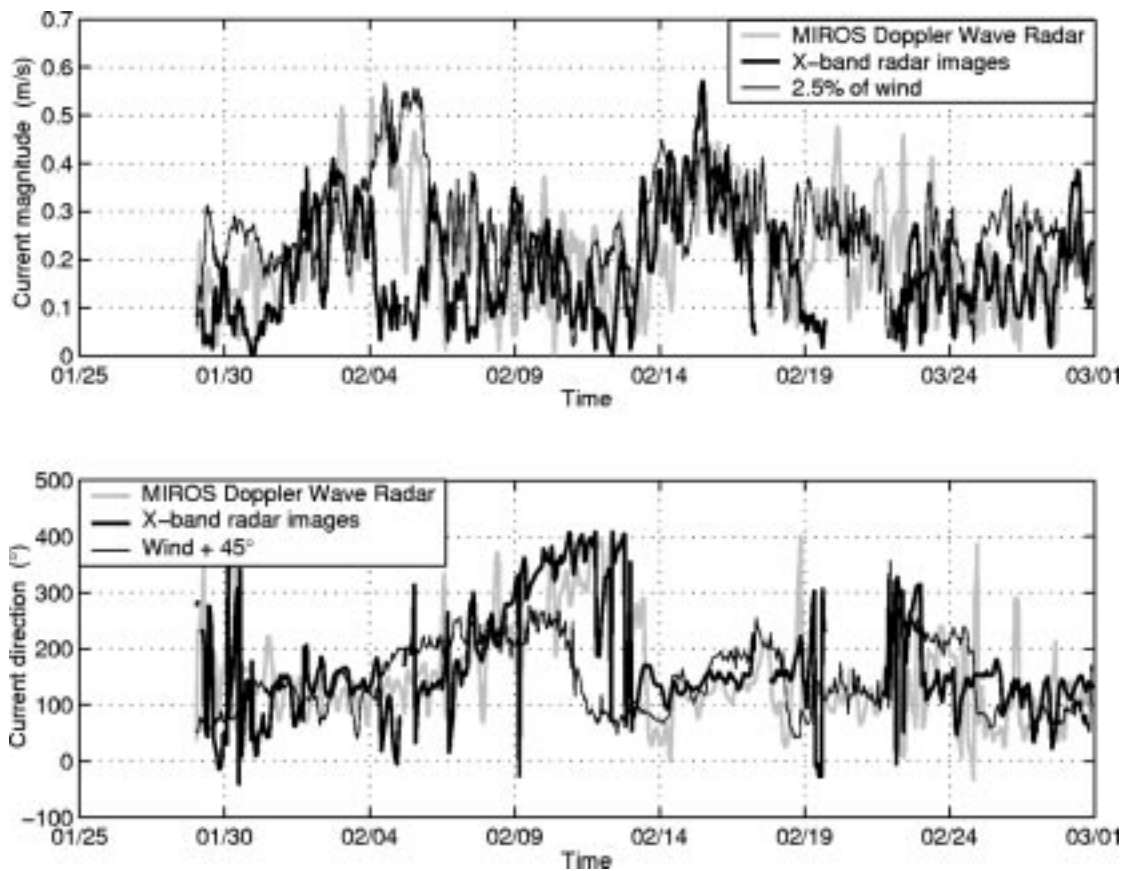


Fig. 2. Estimated X-band radar current data compared to MIROS wave radar and wind data, using Algorithm A with interpolation and noise filtering.

TABLE I
TIDAL MOVEMENT ELLIPSE PARAMETERS FOR THE TIDAL CONSTITUENTS
M2, S2, N2, AND K1. NOTE THAT THE RANGE FOR θ IS $[0^\circ, 180^\circ)$

Tidal constituents			Ellipse parameters			
Symb.	Period	Source	Half axis		θ	Dir.
	(h)		Major (cm/s)	Minor (cm/s)	($^\circ$)	
M2	12.42	Model	8.53	4.13	173	+
		Alg. B	1.56	0.74	179	+
		Alg. A	1.63	0.92	162	+
		W.radar	3.98	2.65	1	+
S2	12.00	Model	2.14	1.15	163	+
		Alg. B	1.05	0.23	157	+
		Alg. A	1.37	0.17	2	-
		W.radar	3.62	0.88	160	+
N2	12.66	Model	2.02	1.02	170	+
		Alg. B	1.70	0.17	173	+
		Alg. A	2.06	0.05	9	+
		W.radar	2.15	1.00	112	+
K1	23.93	Model	2.41	1.13	8	+
		Alg. B	1.41	0.63	136	-
		Alg. A	1.78	0.85	133	-
		W.radar	1.88	0.73	54	-

The tidal constituents are selected in accordance with the length of the time series, by the Rayleigh comparison, as described in [12], and the magnitudes of the constituents at the current location.

It is interesting to compare the estimated currents to the predicted tidal current after filtering the current, using a bandpass

filter to remove some of the current contribution connected to other processes than the tidal motion. Fig. 3 shows a time series of 10 days of data after applying a fourth-order Butterworth bandpass filter [7] with lower cutoff frequency corresponding to 16 h and upper cutoff frequency corresponding to 8 h. Thus, only the semidiurnal tidal band is passing through the filter. The diurnal and long-period tidal band is eliminated, and this is also the case for a great part of the wind driven current. X-band radar current estimated by Algorithm A is indicated with the black line, and predicted tidal current with gray. Only the semidiurnal components of the predicted current are considered. Fig. 4 shows the corresponding time series estimated by Algorithm B. Both magnitudes and phases are corresponding well for both algorithms.

There is a high degree of consistence between the X-band radar and the tidal model current in Figs. 3 and 4. Nevertheless, the deviations in the tidal constituents' amplitudes (Table I) are quite large. A plausible explanation is that the power corresponding to the tidal motion is scattered in an area around the expected frequencies, due to some sort of noise in the direction estimates. Thus, only a small part of the power corresponding to a tidal constituent will be found in the harmonic analysis, because the harmonic analysis is only detecting power in a pre-specified, and very narrow frequency band. Assume the current estimate for a single current constituent for a given time t to be expressed by a magnitude $U(t)$ and a direction $\theta(t)$. The east-west and north-south

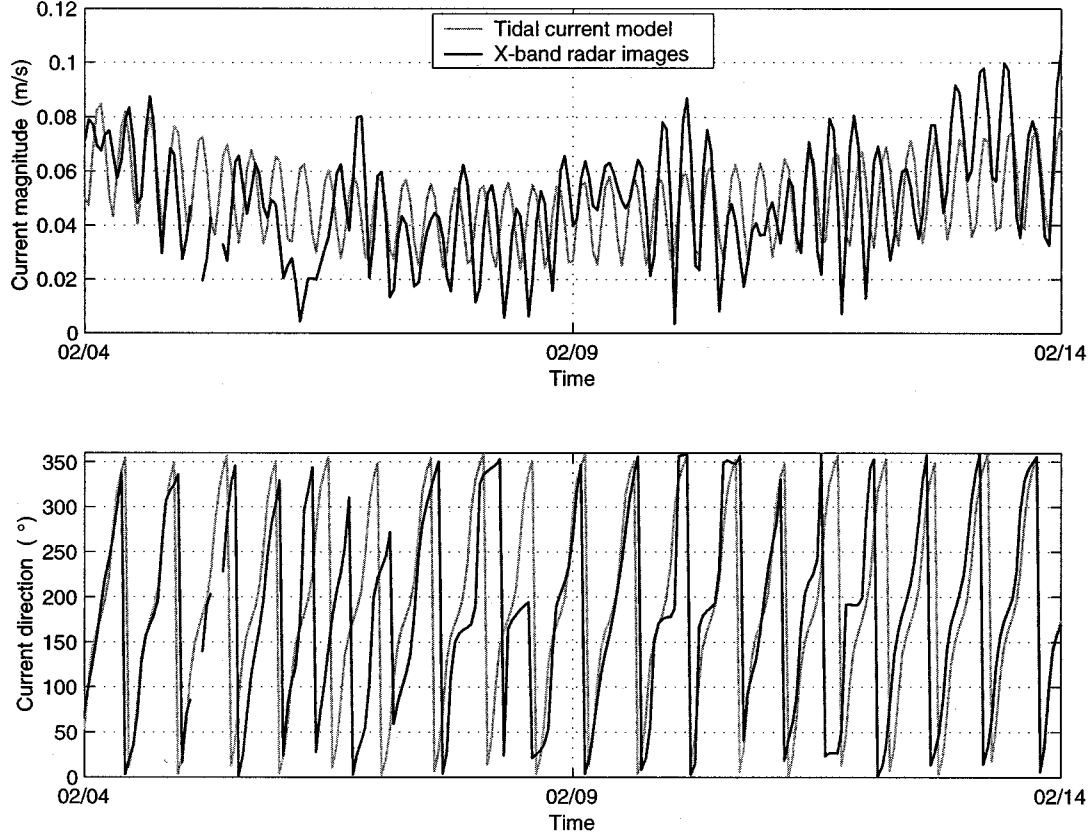


Fig. 3. Estimated X-band radar current time series after applying a bandpass filter, using Algorithm A, compared to predicted semidiurnal tidal current contribution.

components of the tidal current can, respectively, be written [13]

$$u(x, y, t) = u_0(x, y) \cos(\omega t - \delta_u(x, y) + \Psi(t)) \quad (27)$$

and

$$v(x, y, t) = v_0(x, y) \cos(\omega t - \delta_v(x, y) + \Psi(t)) \quad (28)$$

where ω is the tidal constituent frequency, $\delta(x, y)$ is the phase for the current component, and $\Psi(t)$ is the astronomical argument. Investigating the connection between the complex tidal velocity and u and v in [13], it is observed that an error $\Delta\theta(t)$ in the estimated current direction $\theta(t)$ will bring about a corresponding error in the estimates of u and v

$$u_{\text{est}}(x, y, t) = u_0(x, y) \cos(\omega t - \delta_u(x, y) + \Psi(t) + \Delta\theta(t)) \quad (29)$$

and

$$v_{\text{est}}(x, y, t) = v_0(x, y) \cos(\omega t - \delta_v(x, y) + \Psi(t) + \Delta\theta(t)). \quad (30)$$

The error $\Delta\theta(t)$ may for instance be assumed to be normally distributed. The effect of $\Delta\theta(t)$ may be regarded as some sort of phase modulation. Consequently, the frequency spectrum of u_{est} and v_{est} will be scattered in an area around the original frequency ω . Therefore, the power at the original frequency ω will be reduced, in accordance with the observations. The time dependence of $\Psi(t)$ is too weak to cause any significant phase modulation effects in this case.

C. Estimation of the Current Vector Field

Fig. 5 shows a polar X-band radar image collected at the Gullfaks C oil production platform in the North Sea [4] with a WAVEX system [1]. The significant wave height is 4.6 m. The corresponding current vector field estimated with Algorithm A is shown in Fig. 6. The directions of the vector field curl clockwise toward the right image edge. This may be due to an eddy current. The only available reference measurement is an average current estimate from the MIROS wave radar ([5] and [6]), which is indicated in the upper right corner of Fig. 6. The footprint of the MIROS wave radar is located in the left part of the area covered by the polar X-band radar image [4]. The average current over the entire polar image estimated by Algorithm A is indicated in the upper right corner of the figure as well. Taking into account that the MIROS radar is only measuring in the left image part, the agreement between the estimated average current amplitudes and directions for the two measurement techniques is quite good.

Fig. 7 shows the estimated current vector field from the same site as in Fig. 6, one day later. The current direction has changed, and the clockwise curling toward the right image edge has decreased compared to Fig. 6. The significant wave height is 3.4 m.

Taking eddy currents into account, the results obtained from the North Sea may be reasonable. In addition, the vectors of the current vector fields harmonize quite well. It must be emphasized that our knowledge about the current vector field at the site is strongly limited, and that underwater structures belonging

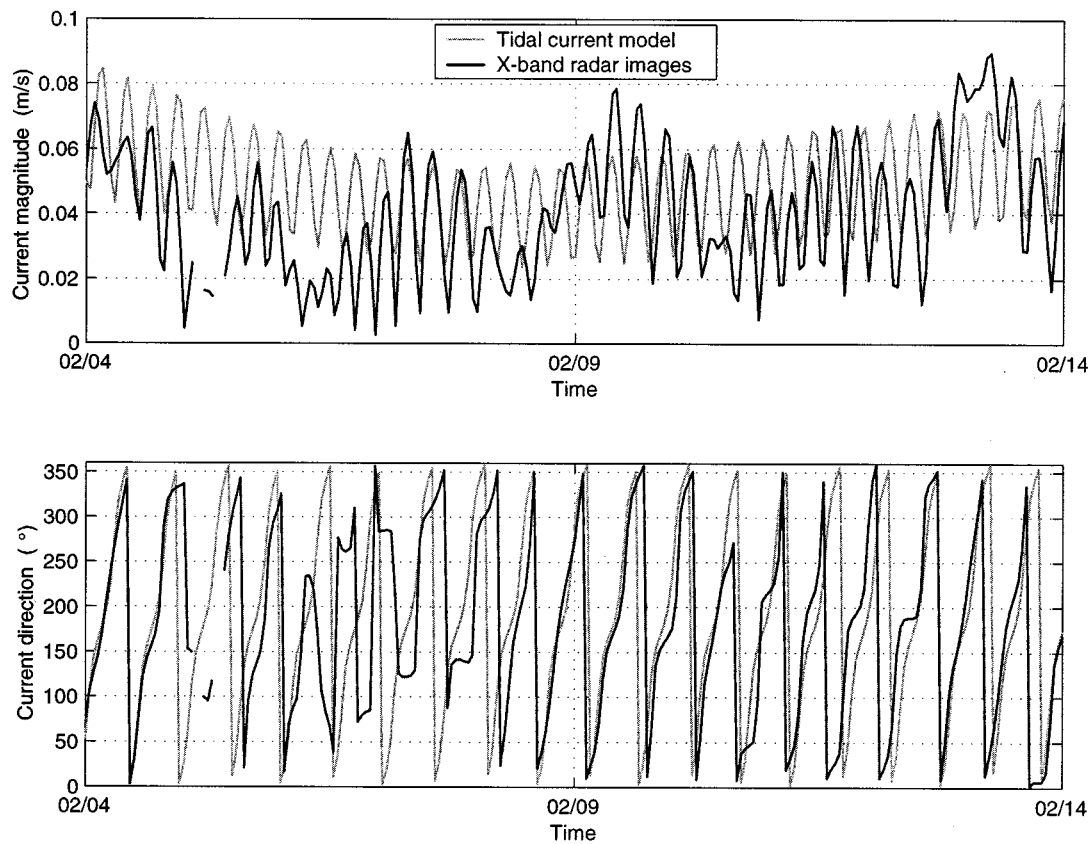


Fig. 4. Estimated X-band radar current time series after applying a bandpass filter, using Algorithm B, compared to predicted semidiurnal tidal current contribution.

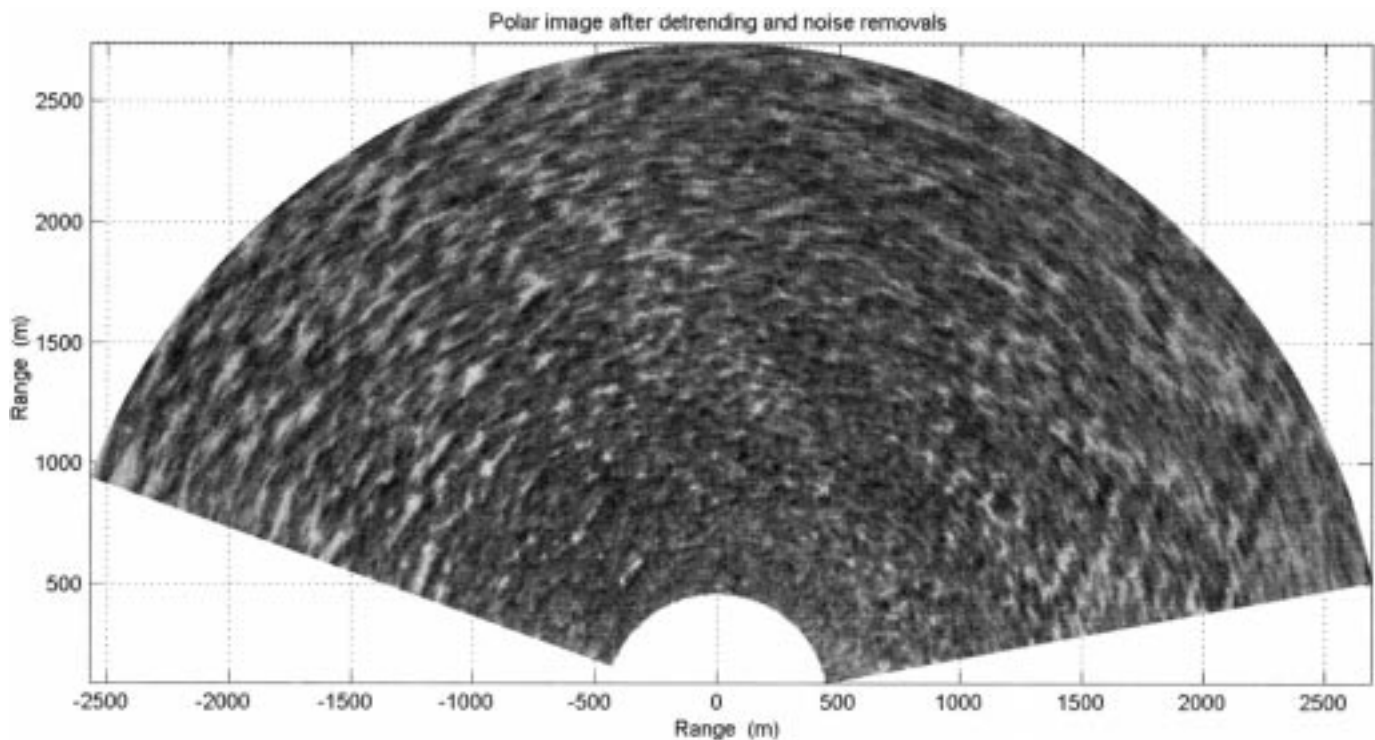


Fig. 5. Polar X-band radar image collected at the Gullfaks C oil production platform in the North Sea.

to the platform may influence the current in the vicinity of the platform.

The results indicate that a current vector field estimate, with resolution of 256 m or better, may be evaluated for a polar area

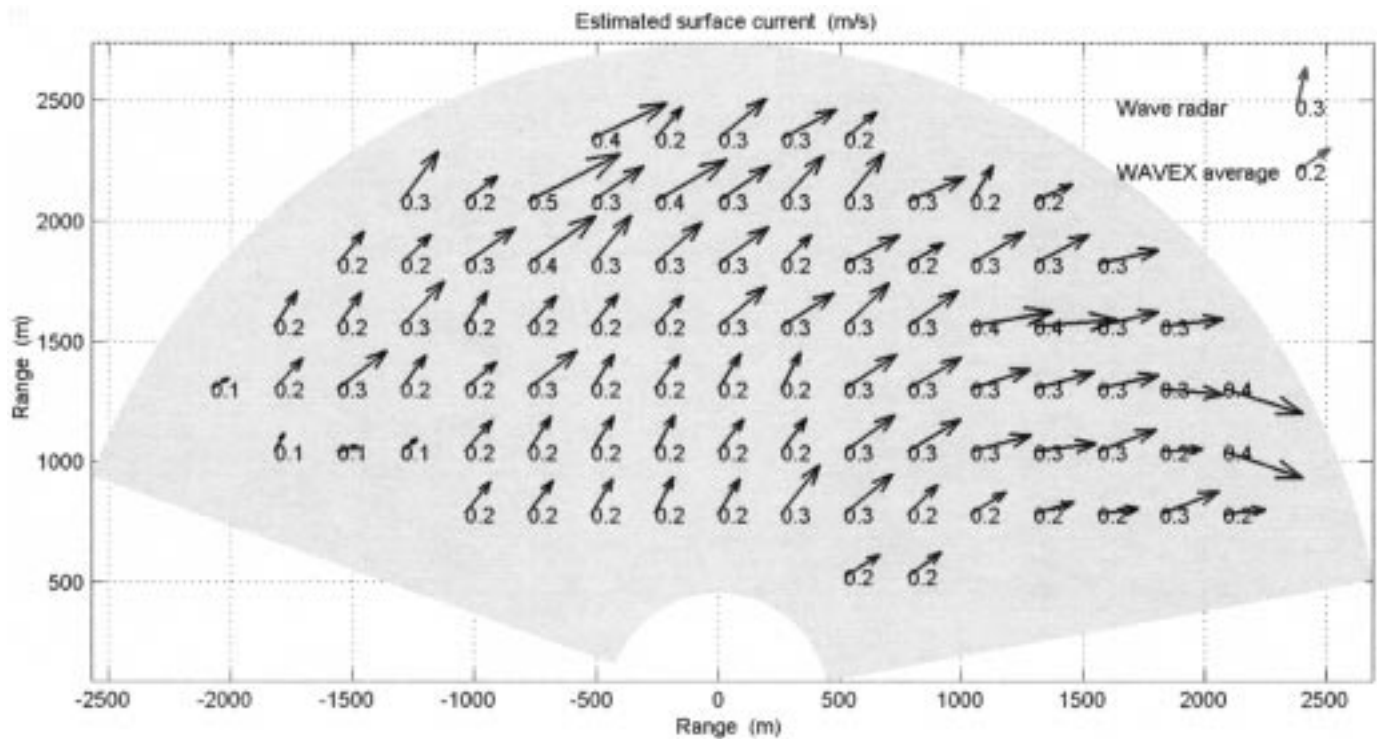


Fig. 6. Estimated current vector field from radar images collected at Gullfaks C in the North Sea.

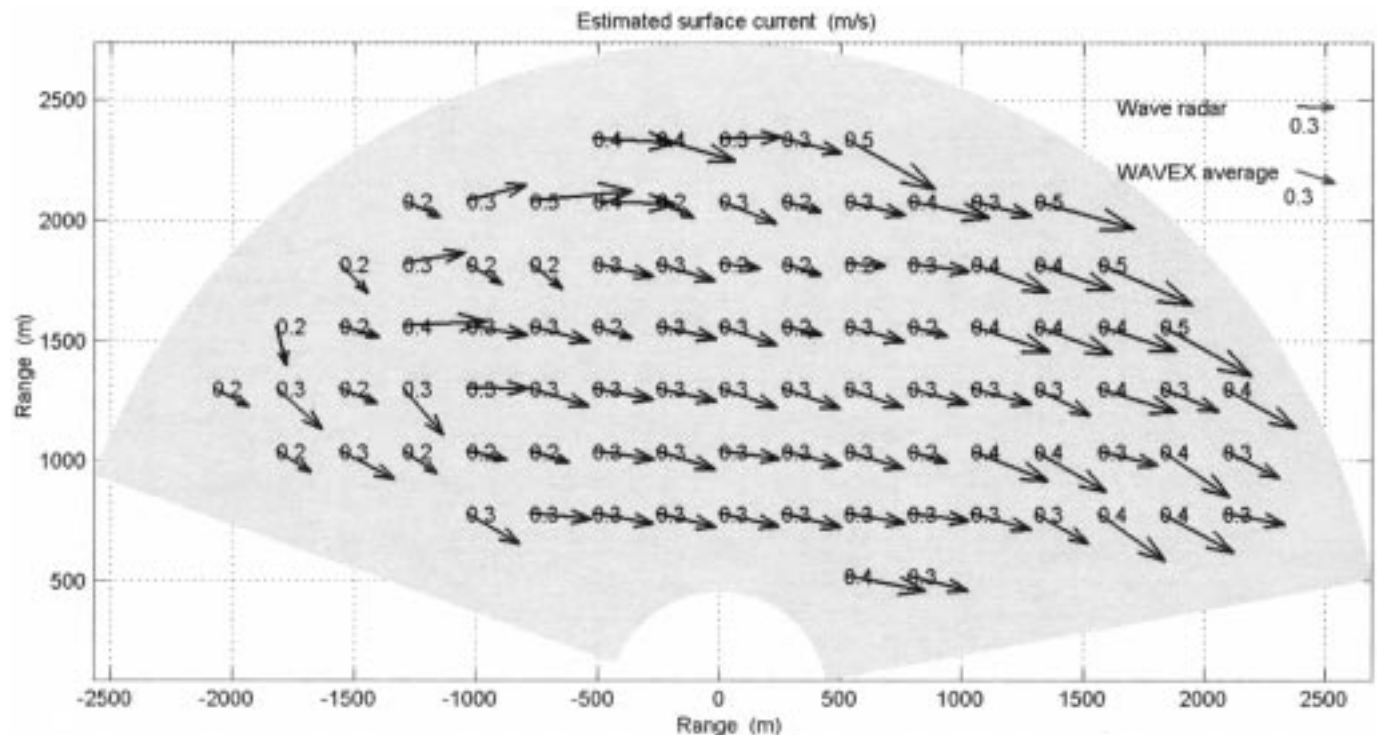


Fig. 7. Estimated current vector field from radar images collected at Gullfaks C.

ranging from 0.5 to 2.5 km. When considering the entire polar image, i.e., 360° , this comes to 19 km^2 .

For estimation of the scaled sea surface wave spectrum from X-band radar images, it is an important task to select an optimal geometry for extracting Cartesian sections from the polar images. This limits the usable area of the polar images.

Previously, the current vector is estimated only in the same Cartesian sections being used for the estimation of the wave spectrum. However, the current estimation algorithms seem to be more robust. Thus, almost the entire polar image can be utilized, and reasonable current estimates can be obtained even in areas where the geometry is not providing reasonable

scaled wave spectrum estimates, as the outer edge of the polar image for instance.

VI. SUMMARY AND CONCLUSION

Sources of errors in connection with estimation of ocean current from X-band radar images are considered. The traditional algorithms of the current estimation are improved (Algorithm A), and tested on real data collected at Gullfaks C in the North Sea.

A novel and alternative algorithm for estimating ocean current from X-band radar sea surface images is described and tested on real data (Algorithm B). One of the reasons for creating this novel algorithm is the possibility to avoid some of the sources of error connected to Algorithm A. However, Algorithm B requires a significantly longer computation time.

The estimated currents are compared to reference data measured by a MIROS Wave Radar (dual-frequency method), wind data, and data from the tidal model. In broad outlines, the consistency of the trends between the X-band radar current values, the wave radar, and the wind is quite good. The consistency between estimated current and tidal current is very good after performing filtering on the data to remove some of the current contributions other than the tidal motion. The angular errors of estimated current ellipses are quite small, but the errors in amplitude are rather high. The explanation of this is probably noise, smearing out the estimated current frequency spectra.

The performance of Algorithm B is very similar to Algorithm A for the test data, despite the fact that several sources of error are avoided using Algorithm B. There seems, however, to be a difference in the estimated tidal constituents. The tidal ellipses' magnitudes of Algorithm B deviate more from the theoretical than the ellipses' magnitudes of Algorithm A, while the angles of the major axis are closer to the theoretical.

No additional noise removal is required when using Algorithm B on the data collected at Gullfaks C. Anyway, if applying Algorithm B on noisy data, there may be a need for noise removal in the future. Robust and reliable noise removal routines may be created for this algorithm, due to the possibility of comparing the predicted power frequency spectrum for every wavenumber bin to the measured spectrum.

It seems to be possible to estimate the sea surface current vector field over an area of many square kilometers, with a resolution of 256 m or better, using images from one single fixed X-band radar. The method is tested on real X-band radar images from the North Sea, and the results seem to be reasonable. The agreement between the average current vector estimated from the X-band radar images and a reference Doppler radar is quite good.

ACKNOWLEDGMENT

The author would like to thank Ø. Grønlie for providing excellent supervision during the project and for generously sharing his vast knowledge, E. Nøst for providing highly qualified support on technical and literary work and providing data from the tidal model, and R. A. Jørgensen and M. Evans for their helpful suggestions regarding the language of the manuscript.

REFERENCES

- [1] Ø. Grønlie, "WAVEX—Principles of Operation," MIROS, GD/007/98/ØG/1300/D, 1998.
- [2] I. R. Young, W. Rosenthal, and F. Ziemer, "A three-dimensional analysis of marine radar images for the determination of ocean wave directionality and surface currents," *J. Geophys. Res.*, vol. 90, no. C1, pp. 1049–1059, Jan. 1985.
- [3] P. Skaaren-Fystro, "Examination and Analysis of the WAVEX System for the Processing of Radar Pictures," Diploma, Univ. Trondheim, Norway, 1991.
- [4] R. Gangeskär, "Collecting Digitized Radar Images at Gullfaks C 1998–1999," MIROS, 1300/DD/003, 1999.
- [5] T. Eide, "MIROS Wave Radar MkII—Principles of Operation," MIROS, GD/014/92/ØG/6112/P, 1996.
- [6] —, "Wave Radar MkII—System Module," MIROS, SM/001, 1999.
- [7] A. V. Oppenheim and R. W. Schaffer, *Discrete-Time Signal Processing*. Englewood Cliffs, NJ: Prentice-Hall, 1989.
- [8] D. H. Johnson and D. E. Dudgeon, *Array Signal Processing: Concepts and Techniques*. Englewood Cliffs, NJ: Prentice-Hall, 1993, pp. 59–106.
- [9] B. Kinsman, *Wind Waves, Their Generation and Propagation on the Ocean Surface*. Englewood Cliffs, NJ: Prentice-Hall, 1965, p. 341.
- [10] K. L. Lavalli. (2001) Ocean Circulation I: Wind Induced Circulation. Southwest Texas State University. [Online]. Available: <http://www.bio.swt.edu/Lavalli/oceans/lectures/circulation1.html>
- [11] B. Gjevik, E. Nøst, and T. Straume, "Atlas of Tides on the Shelves of the Norwegian and the Barents Tides," Statoil, Stavanger, Norway, F&U-ST 90012, 1990.
- [12] W. J. Emery and R. E. Thomson, *Data Analysis Methods in Physical Oceanography*, 1 ed. New York, 1998.
- [13] E. Nøst, "Tidal Currents Near the Critical Latitude in the Barents Sea," Dr. Sci. thesis, Univ. Oslo, Norway, 1994.



Rune Gangeskär received the Cand.Sci. and Dr.Sci. degrees in physics and instrumentation from the University of Oslo, Norway, in 1995 and 2002, respectively.

He was a Research Scientist for SINTEF Electronics and Cybernetics from 1995 to 1998. Since 1998, he has been with MIROS A/S, Asker, Norway, as a Research Fellow, developing algorithms for the WAVEX system for estimating wave spectra and ocean currents from radar images.